



Cite this: *Energy Adv.*, 2024, 3, 1956

## Exploration of bismuth-based materials for photocatalytic decomposition of $\text{N}_2\text{O}$ †

Shalu Atri, <sup>\*a</sup> Sentharaman Uma, <sup>b</sup> Rajamani Nagarajan, <sup>b</sup> Maros Gregor, <sup>c</sup> Tomas Roch, <sup>c</sup> Miroslava Filip Edelmannova, <sup>d</sup> Martin Reli, <sup>d</sup> Kamila Koci, <sup>d</sup> Martin Motola and Olivier Monfort <sup>\*a</sup>

This work is focused on the investigation of three different Bi-based materials, *i.e.*,  $\text{CaBi}_2\text{O}_2(\text{CO}_3)_2$  (CBOC),  $\text{Ca}_4\text{Bi}_6\text{O}_{13}$  (CBO), and  $\text{Bi}_2\text{Ce}_2\text{O}_7$  (BCO), as photocatalysts in  $\text{N}_2\text{O}$  reduction. This study has emphasized the effectiveness of the bismuth ion, irrespective of its presence in different structures with self-regulating electronic and morphological properties, when employed as a photocatalyst. Monophasic CBOC, CBO, and BCO samples have been synthesized by wet-chemical methods, and they exhibit distinct morphological features such as plate-like, dumbbell-shaped, and irregularly shaped crystallites. From the UV-visible diffuse reflectance spectroscopy (DRS) data, CBO exhibits a lower optical band gap of 2.52 eV compared to CBOC (3.95 eV), which CBO is synthesized from. BCO shows the lowest optical band gap of 2.16 eV. CBO exhibits the highest photocurrent generation and the lowest value in work function measurements, following the trend as CBO > CBOC > BCO. The efficiency of the Bi-based materials in photocatalytic decomposition of  $\text{N}_2\text{O}$  also follows a similar trend as observed in the photocurrent measurements, wherein the CBO sample exhibits a maximum of 10.4% decomposition of  $\text{N}_2\text{O}$  under UV-A in 24 h. Oxygen vacancies in CBO and BCO have been reasoned to play a crucial role in the photocatalytic decomposition of  $\text{N}_2\text{O}$ .

Received 15th April 2024,  
Accepted 17th June 2024

DOI: 10.1039/d4ya00240g

rsc.li/energy-advances

## Introduction

Presently, greenhouse gases are a global challenge; one of the prominent causes is the generation of hazardous gases by the combustion of fossil fuels. Among these gases,  $\text{N}_2\text{O}$  has 310 times higher potential than  $\text{CO}_2$  to contribute to global warming.<sup>1</sup> There are different approaches to reduce  $\text{N}_2\text{O}$  emission from industry such as direct catalytic decomposition or thermal decomposition.<sup>2–7</sup> However, all of them require significant energy inputs which limits their wide utilizations.<sup>2–7</sup> On the other hand, photocatalytic decomposition of  $\text{N}_2\text{O}$  under UV or visible light irradiation using semiconductors can be a

promising approach involving renewable energy resources.<sup>8</sup>  $\text{TiO}_2$ , a well-known semiconductor photocatalyst, has been examined for its efficacy in decomposing  $\text{N}_2\text{O}$ . However, the wide band gap and fast recombination of charge carriers should be addressed by designing solar light-driven photocatalysts.<sup>9–12</sup> Indeed, the use of natural sunlight, which is composed of visible and UVA light, is crucial to achieve a sustainable and cost-effective photocatalytic process, thus making it more environmentally friendly.

$\text{Bi}_2\text{O}_3$  is an interesting photocatalyst as it holds a narrow band gap, thus being activated by visible light.<sup>13</sup> Previously reported studies have shown that the morphology and microstructure of  $\text{Bi}_2\text{O}_3$  are interrelated to exhibit high photocatalytic activity.<sup>14–16</sup> Furthermore, it is well known that doping in the  $\text{Bi}_2\text{O}_3$  system resulted in a red shift to the absorption edge, which attracted high attention of researchers to utilize them for photocatalytic application.<sup>17</sup> Indeed, cerium is known to exhibit active redox behaviour with fast interconvertible  $\text{Ce}^{4+}$  to  $\text{Ce}^{3+}$  oxidation states, which supports transport variation in oxygen concentration and thereby helps to improve photocatalytic efficiency.<sup>18–21</sup> Also, other bismuth-based photocatalysts *e.g.*,  $\text{BiOIO}_3$ ,  $\text{Bi}_2\text{SnO}_7$ ,  $\text{Bi}_2\text{O}_2(\text{CO}_3)_2$ ,  $\text{BiFeO}_3$ ,  $\text{BiVO}_4$ ,  $\text{Bi}_2\text{WO}_6$ , and  $\text{BiOBr}$  achieved a huge popularity due to their unique electronic structure, tuneable surface properties and appropriate band gap.<sup>22–24</sup> The reported studies illustrate the potential of bismuth-based materials as efficient catalysts for  $\text{N}_2\text{O}$  decomposition.<sup>22,23,25</sup>

<sup>a</sup> Comenius University Bratislava, Faculty of Natural Sciences, Department of Inorganic Chemistry, Ilkovicova 6, Mlynska Dolina, 84215 Bratislava, Slovakia.

E-mail: shalu1@uniba.sk, olivier.monfort@uniba.sk

<sup>b</sup> Materials Chemistry Group, Department of Chemistry, University of Delhi, 110007 Delhi, India

<sup>c</sup> Comenius University Bratislava, Faculty of Mathematics Physics and Informatics, Centre for Nanotechnology and Advanced Materials, Mlynska Dolina, 84248 Bratislava, Slovakia

<sup>d</sup> VSB – Technical University of Ostrava, Centre of Energy and Environmental Technologies, Institute of Environmental Technology, 17. listopadu 2172/15, 70800 Ostrava-Poruba, Czech Republic

† Electronic supplementary information (ESI) available: Figure for BET, photocurrent measurements, XPS wide spectra and  $\text{N}_2\text{O}$  decomposition under UV-C irradiation. See DOI: <https://doi.org/10.1039/d4ya00240g>



For example, 85% decomposition of  $\text{N}_2\text{O}$  was achieved in 30 minutes using  $\text{Bi}_2\text{MoO}_6$ , 90% in 45 minutes using  $\text{BiVO}_4$ , and 95% in 60 minutes using  $\text{BiFeO}_3$ .<sup>22,23,25</sup> Although these materials can operate at lower temperatures and exhibit high time stability, further improvements can be reached by optimizing the synthesis conditions of the bismuth-based photocatalysts. DFT studies demonstrated that Bi 6s and O 2p orbitals undergo a powerful hybridization and resulted in a high dispersion in valence band, thus shifting the energy band gap to lower energy compared to most of the other photocatalysts.<sup>26</sup> Additionally, bismuth-based materials can be prepared by facile and cost-effective methods.<sup>27</sup> The photocatalytic performance of bismuth-based materials is independent of the type of crystal structure, and it can be attributed to the bismuth ion and the stereo-chemically active lone pair associated with it, reducing the charge carriers' recombination rate.<sup>28–30</sup>

In this context, the current study is designed to assess the impact of different chemical structures and compositions of bismuth-based materials ( $\text{CaBi}_2\text{O}_2(\text{CO}_3)_2$ ,  $\text{Ca}_4\text{Bi}_6\text{O}_{13}$ , and  $\text{Bi}_2\text{Ce}_2\text{O}_7$ ) on the photocatalytic decomposition of  $\text{N}_2\text{O}$ . The idea behind the selection of these specific materials is motivated by several facts: (i) in  $\text{CaBi}_2\text{O}_2(\text{CO}_3)_2$ , the presence of carbonate groups along with bismuth and calcium might affect interestingly the photocatalytic properties;<sup>31,32</sup> (ii) the different crystal structures between  $\text{Ca}_4\text{Bi}_6\text{O}_{13}$  and  $\text{CaBi}_2\text{O}_2(\text{CO}_3)_2$ , along with their different Ca:Bi ratio might lead to a better understanding of the role of these element on the material's properties (in addition,  $\text{Ca}_4\text{Bi}_6\text{O}_{13}$  can be synthesized directly from  $\text{CaBi}_2\text{O}_2(\text{CO}_3)_2$ );<sup>33</sup> and (iii) by replacing calcium with cerium *i.e.* from  $\text{Ca}_4\text{Bi}_6\text{O}_{13}$  to  $\text{Bi}_2\text{Ce}_2\text{O}_7$ , the specific impact of Ce over Ca on the photocatalytic properties might be clarified. Furthermore, the redox behaviour of cerium in bismuth materials can provide a greater number of active sites, thus facilitating electron transfer and ultimately the photocatalytic properties.<sup>34</sup> With this approach, the comparative study of these three distinct Bi-based materials will highlight how different chemical structures and compositions influence photocatalytic efficiency in  $\text{N}_2\text{O}$  removal under UVA. It is worth highlighting that our report is the first investigation delving into the photocatalytic assessment of these systems for the decomposition of  $\text{N}_2\text{O}$ .

## Results and discussion

### Crystalline structure and morphology of Bi-based materials

The XRD analysis of CBOC, CBO, and BCO confirmed crystalline  $\text{Ca}_2\text{Bi}_2\text{O}_2(\text{CO}_3)_2$ ,  $\text{Ca}_4\text{Bi}_6\text{O}_{13}$ , and  $\text{Bi}_2\text{Ce}_2\text{O}_7$ , respectively, in accordance with previous findings (Fig. 1).<sup>35–37</sup> Lattice refinements by the Le Bail method yielded lattice dimensions of CBOC, CBO and BCO as follows: CBOC (beyerite, *Immm* S.G.)  $a = 3.771(1)$ ,  $b = 3.770(1)$ ,  $c = 21.724(2)$  Å; CBO ( $\text{Ca}_4\text{Bi}_6\text{O}_{13}$ ) obtained by thermolysis of beyerite (*C2mmm* S.G.)  $a = 17.377(3)$ ,  $b = 5.940(1)$ ,  $c = 7.225(1)$  Å and BCO ( $\text{Bi}_2\text{Ce}_2\text{O}_7$ ) (fluorite, *Fm\bar{3}m*)  $a = b = c = 5.479(4)$  Å, which confirmed the purity of the materials.<sup>35–37</sup> Interestingly, CBO, obtained from the thermolysis of CBOC, is not a typical phase. Indeed, previous reports

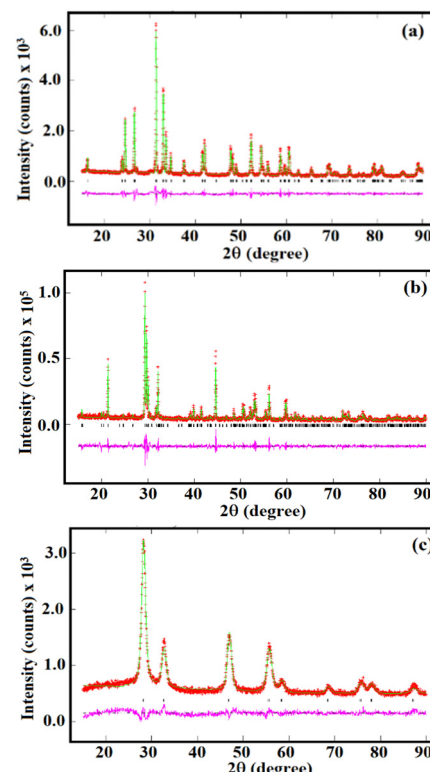


Fig. 1 Lattice refinements of the PXRD patterns of (a) CBOC, (b) CBO, and (c) BCO by the Le Bail method. The red, green, and pink lines are for the experimental data, the calculated, and the difference profiles, respectively.

claimed that the thermolysis of CBOC leads to the formation of metastable  $\text{CaBi}_2\text{O}_4$ .<sup>35,38</sup> However, in our case, reducing calcination time at the same temperature aided the formation of  $\text{Ca}_4\text{Bi}_6\text{O}_{13}$ . Also, using different precursors for synthesizing CBOC compared to these reports might have played a crucial role in stabilizing the  $\text{Ca}_4\text{Bi}_6\text{O}_{13}$  phase. Additionally, prolonged heat treatment at higher temperatures is avoided, constituting a significant advantage of low temperature synthesis of monophasic  $\text{Ca}_4\text{Bi}_6\text{O}_{13}$ .<sup>37</sup> The formation of the  $\text{Ca}_4\text{Bi}_6\text{O}_{13}$  phase from CBOC proved its versatility in producing metastable oxides containing calcium and bismuth. The CBOC crystallites have a plate-like morphology (Fig. 2a),<sup>35</sup> while for CBO obtained by the thermolysis of CBOC, the morphology of the crystallites changed from plate-like to dumbbell-shaped with porous morphology (Fig. 2b).

To explain this observation, the CBOC structure typically involves layers of Bi–O and carbonate groups that can promote plate-like morphologies due to the anisotropic nature of the bonding in the structure. The strong bonding within the layers and weaker interactions between them can lead to preferential growth along certain crystallographic directions, resulting in plate-like structures. On the other hand, CBO has a more complex structure, with multiple calcium and bismuth sites in the oxygen frameworks. This complexity can result in different crystallographic planes having different growth rates, leading to varied morphologies such as dumbbell-shaped or irregular crystallites. Concerning BCO, the irregularly shaped crystallites

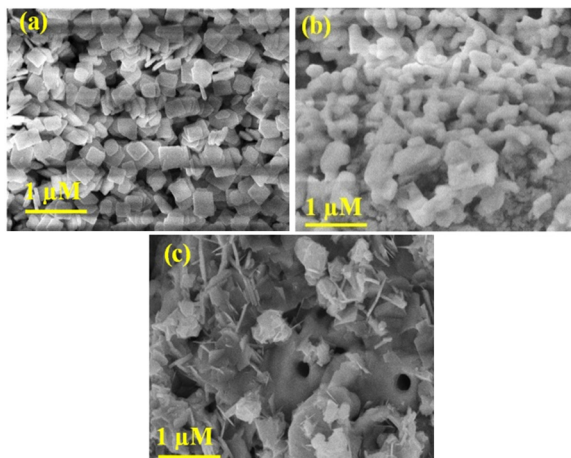


Fig. 2 SEM images for (a) CBOC, (b) CBO, and (c) BCO.

(Fig. 2c) are in accordance with previous reports.<sup>36</sup> Such a morphology can be due to several factors related to synthesis conditions. The average crystallite sizes, calculated using Scherrer analysis, were 45 nm (CBOC), 70 nm (CBO) and 8 nm (BCO).

Fig. S1 (ESI†) shows the  $N_2$  adsorption–desorption BET surface area isotherm curves, wherein a type-II adsorption for CBOC and CBO samples suggested mainly macro-porous behaviour of the materials. This behaviour can be attributed to their structural characteristics, wherein the presence of calcium and bismuth leads to larger interstitial sites than tightly bound micro- and meso-pores. While a type-IV isotherm is observed for the BCO sample, it demonstrated its mesoporous nature arising from its synthesis method which is different to that of CBOC and CBO.<sup>39</sup>

The observed specific surface areas for the CBOC, CBO and BCO samples are 22, 5.5 and  $41\text{ m}^2\text{ g}^{-1}$ . According to Table 1, the maximum value of adsorbed monolayer is observed for the BCO sample, thus being beneficial for its heterogeneous photocatalytic performance.<sup>40–44</sup> For CBOC and CBO samples, the BET analysis suggested a predominantly low mesoporous character with some micropores but mainly macropores. On the other hand, the BCO sample has a predominantly mesoporous character with some micropore and macropore representation (Table 1).

DRS is recorded and reproduced in Fig. 3. The corresponding Tauc plots are shown as insets in Fig. 3. The estimated optical band gap ( $E_g$ ) value for CBOC is 3.95 eV (Fig. 3a), which is in accordance with the value reported in the literature.<sup>35</sup> The absorbance edge for the CBO and BCO samples falls at the edge

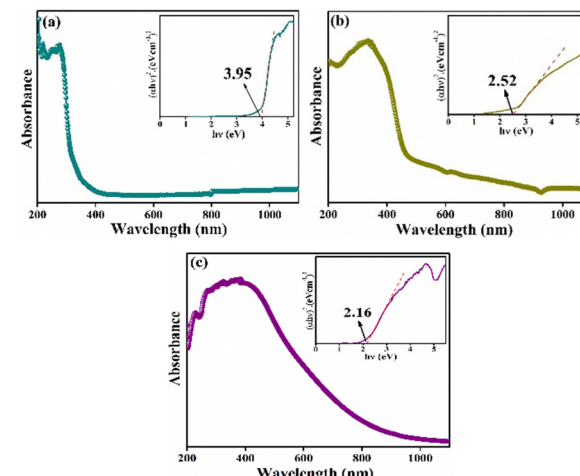


Fig. 3 DRS spectra of (a) CBOC, (b) CBO, and (c) BCO. Inset shows the respective Tauc plot.

of the UV-visible junction (Fig. 3b and c), which is evident due to the yellow colors of the samples. In the case of CBO, a significant reduction in  $E_g$  and slight lift in the absorption tail and extended up to visible region (Fig. 3b) suggested the presence of defects and oxygen vacancies.<sup>37</sup> The difference in optical properties between CBOC and CBO arose from different structural and chemical compositions, thus leading to different electronic band structures. The  $E_g$  of BCO (2.16 eV) matches well with the literature.<sup>36</sup> The smaller value of  $E_g$  for BCO among the three samples, is due to inclusion of Ce and its f-orbitals, which can interact with the existing electronic states, thereby modifying the electronic band structure and reducing the  $E_g$ .

### Photoelectrochemical performance

The photocurrent data recorded as a function of wavelength and applied potential are reported in Fig. S2 (ESI†). The blue areas represent cathodic photocurrent, while the red ones are for anodic photocurrent. All the samples showed low cathodic photocurrent, detected at low applied potential. On the other hand, higher anodic photocurrent values were obtained at higher applied voltage, and CBO showed photocurrent values 4.5-fold and 10-fold higher at 1 V than for CBOC and BCO, respectively (Fig. 4 and Fig. S2 (ESI†)). As per the reported literature, the high value of photocurrent arises either due to efficient transport of electrons or longer life of generated charge carriers.<sup>45</sup> In Fig. 4, the transient photocurrent was obtained using a shutter, which was opened for 5 s and closed

Table 1 Characteristic parameters for CBOC, CBO and BCO samples from BET analysis

Sample identification	$a\text{ [m}^2\text{ g}^{-1}\text{]}$	$b\text{ [cm}^3\text{ g}^{-1}\text{]}$	$c\text{ [cm}^3\text{ g}^{-1}\text{]}$	$d\text{ [cm}^3\text{ g}^{-1}\text{]}$	$e\text{ [cm}^3\text{ g}^{-1}\text{]}$	$f$
BCO	<sup>+</sup> 41	<sup>+</sup> 9.3	0.114	0.014	0.127	ME, less MI, with little MA
CBOC	<sup>+</sup> 22	<sup>+</sup> 5.1	0.034	0.006	0.032	Little ME, less MI, with more MA
CBO	<sup>+</sup> 5.5	<sup>+</sup> 1.3	0.010	0.002	0.011	Little ME, less MI, with more MA

$a$  – specific surface area according to BET<sup>40</sup> – marked+;  $b$  – volume of the adsorbed monomolecular layer;  $c$  – cumulative pore volume according to Gurvich;<sup>41</sup>  $d$  – cumulative volume of micropores (MI) according to Horvath–Kawazoe;<sup>42</sup>  $e$  – cumulative volume of mesopore (ME) and macropore (MA) according to BJH method;<sup>43,44</sup>  $f$  – nature of the material.



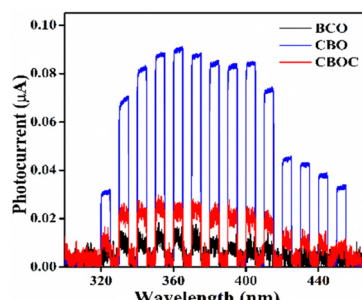


Fig. 4 Photocurrent generation at different wavelengths by applying 1 V and using 5 s open/close shutter.

for 5 s. The current instantly reaches a plateau when the shutter opens and drops immediately to zero when the shutter closes, thus highlighting a clear photo effect and suggesting a fast charge carrier transfer.

The IPCE was also studied at different wavelengths and 1 V (Fig. 5a) and at different applied potentials at 350 nm (Fig. 5b). The higher values of IPCE at 1 V in the UVA region, *i.e.*, from 320 nm to 380 nm, indicated that the three Bi-based materials could be activated under UVA light (Fig. 5a). By increasing the voltage from 0 to 1 V at 350 nm, the IPCE is found to be at its maximum at 1 V (Fig. 5b), but the applied potential effect was insignificant in CBOC and BCO. In other words, the applied voltage was significantly higher in the case of CBO, where the IPCE reached 0.4%.

The work function of the three samples was calculated since a smaller value of the work function usually facilitates redox processes taking place during  $\text{N}_2\text{O}$  decomposition.<sup>46</sup> The calculated work function for each sample (Table 2) was directly correlated with their photoelectrochemical performance, *i.e.*, the smallest work function was obtained for CBO (5.15 eV), which showed higher photocurrent in the UVA region. To summarize, the order of work function and IPCE (at different wavelengths and potentials) is as follows: CBO > CBOC > BCO. Therefore, CBO was further used in the photocatalytic decomposition of  $\text{N}_2\text{O}$ .

### Photocatalytic decomposition of $\text{N}_2\text{O}$

All three samples were subjected to preliminary tests of  $\text{N}_2\text{O}$  decomposition under UV-C light (Fig. S3 (ESI<sup>†</sup>)). The photocatalytic decomposition of  $\text{N}_2\text{O}$  follows the order of CBO > BCO  $\approx$  CBOC. As CBO shows higher photocatalytic ability, the

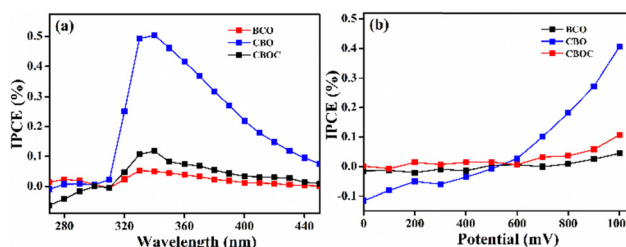


Fig. 5 IPCE measurements at (a) fixed applied potential 1 V and (b) fixed wavelength 350 nm.

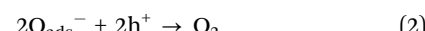
Table 2 Work function of the measured samples

Sample	Work function (eV)
BCO	$5.27 \pm 0.01$
CBO	$5.15 \pm 0.01$
CBOC	$5.20 \pm 0.02$

decomposition of  $\text{N}_2\text{O}$  is also investigated under UV-A (Fig. 6), as it is the region where it shows the best photoelectrochemical performance (see previous section). For reference,  $\text{N}_2\text{O}$  photolysis under UVA irradiation has shown negligible conversion rate.<sup>47</sup> The CBO photocatalyst demonstrated 10.4% decomposition of  $\text{N}_2\text{O}$  under UV-A irradiation ( $\lambda_{\text{max}} = 365 \text{ nm}$ ). Although CBO can be considered a moderate photocatalyst compared to other semiconductor materials under similar sets of reaction conditions *e.g.*,  $\text{g-C}_3\text{N}_4$ ,  $\text{TiO}_2$ , *etc.*<sup>48–50</sup> it is utilized for the first time for  $\text{N}_2\text{O}$  decomposition and it might be a promising material for the preparation of composite and doped systems.

### Plausible mechanism

Based on previously published reports,<sup>51</sup> there are mainly two factors that facilitate the photocatalytic decomposition of  $\text{N}_2\text{O}$  at the surface of the photocatalyst: the reduction of  $\text{N}_2\text{O}$  into  $\text{N}_2$  (eqn (1)) and the oxidation of adsorbed oxygen species into  $\text{O}_2$  (eqn (2) and (3)). The photocatalytic decomposition involves the reduction of  $\text{N}_2\text{O}$ . In addition, hydroxyl groups can react readily with holes and thereby restrict the recombination of charge carriers,<sup>51–53</sup> while the oxygen vacancies present serve as active sites that easily adsorb oxygen species.<sup>54</sup>



The plausible mechanism of CBOC, CBO, and BCO is following the conventional mechanism, *i.e.*, as in eqn (1)–(3) (Fig. 7). Since CBOC has a layered structure, the areas between the layers can behave as the active centers for the photocatalytic reaction.<sup>27</sup> The higher performance of CBO could be ascribed to their mesoporous and macroporous nature and generation of oxygen vacancies/defects since its preparation from CBOC is accompanied by the evolution of  $\text{CO}_2$  gas.<sup>38</sup> It has been determined in a previous study that thermolysis of CBOC

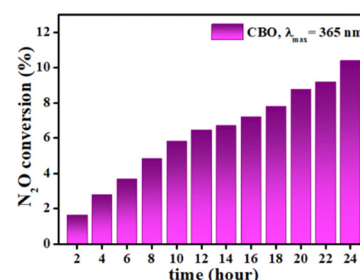


Fig. 6 Time dependence on the  $\text{N}_2\text{O}$  conversion during the photocatalytic decomposition of  $\text{N}_2\text{O}$  over CBO under UV-A irradiation at 365 nm.



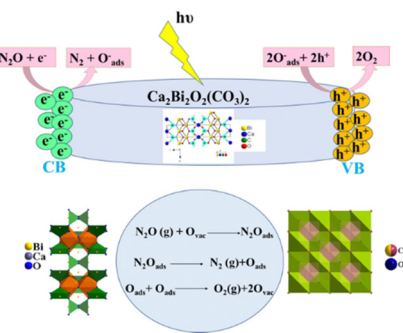
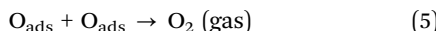
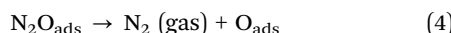


Fig. 7 Plausible mechanism for photocatalytic decomposition of  $\text{N}_2\text{O}$  using Bi-based photocatalysts.

resulted in stabilization of the mesoporous material with enriched oxygen vacancies, which has been confirmed by Raman investigations.<sup>51,53</sup> In addition, we reported earlier that oxygen vacancies played a major role to enhance the catalytic properties of BCO.<sup>36</sup> Therefore, it is expected that the oxygen vacancy sites at the surface of CBO and BCO can bind with the oxygen of  $\text{N}_2\text{O}$  and initiate the decomposition of  $\text{N}_2\text{O}$  as described in eqn (4) and (5).<sup>55</sup> The pictorial representation of the plausible mechanism is provided in Fig. 7.



The study of the surface chemistry on CBOC, CBO and BCO samples before and after  $\text{N}_2\text{O}$  decomposition was performed by using XPS to support the proposed mechanism. The consistency in the peak positions in the wide spectra of Bi, Ca, C, O (in CBOC and CBO) and Bi, Ce, O (in BCO) before and after  $\text{N}_2\text{O}$  decomposition highlights the stability of the photocatalysts (Fig. S4) (ESI†). In the high resolution XPS spectra of the Bi 4f orbitals of the three samples (Fig. 8a–c), the splitting of Bi 4f<sub>7/2</sub> and Bi 4f<sub>5/2</sub> into multiple components after  $\text{N}_2\text{O}$  decomposition is due to spin orbital coupling and redox behaviour of bismuth. Before  $\text{N}_2\text{O}$  decomposition, an additional Bi 4f peak appears in CBOC compared to CBO and BCO and it corresponds to the presence of Bi–O and Bi–C bonds.<sup>56</sup> After  $\text{N}_2\text{O}$  decomposition, the Bi 4f peaks corresponding to  $\text{Bi}^{5+}$  appear, thus confirming that  $\text{Bi}^{3+}$  is oxidized upon  $\text{N}_2\text{O}$  decomposition (Fig. 8a–c).<sup>57,58</sup> Concerning the O 1s spectra, a sharp peak encountered at 530.7 eV can be attributed to lattice oxygen in CBOC, while peaks at higher binding energies of 532.4 and 534.2 eV correspond to –OH and carbonate groups present in the structure before  $\text{N}_2\text{O}$  decomposition (Fig. 8d). The disappearance of the peak corresponding to the –OH group suggests that the photocatalytic reactions involved hydroxyl groups.<sup>51</sup> In the CBO and BCO samples, the peaks at 529.3 eV and 529.0 eV represent the lattice oxygen while surface adsorbed water molecules are identified at 532.8 eV. A significant amount of oxygen vacancies was observed at 531.3 eV and 531.0 eV in the CBO and BCO, respectively (Fig. 8e and f).<sup>59</sup> The presence of C=O groups in the samples might be due to residue left from the precursor during the synthesis conditions. Among the three samples, it

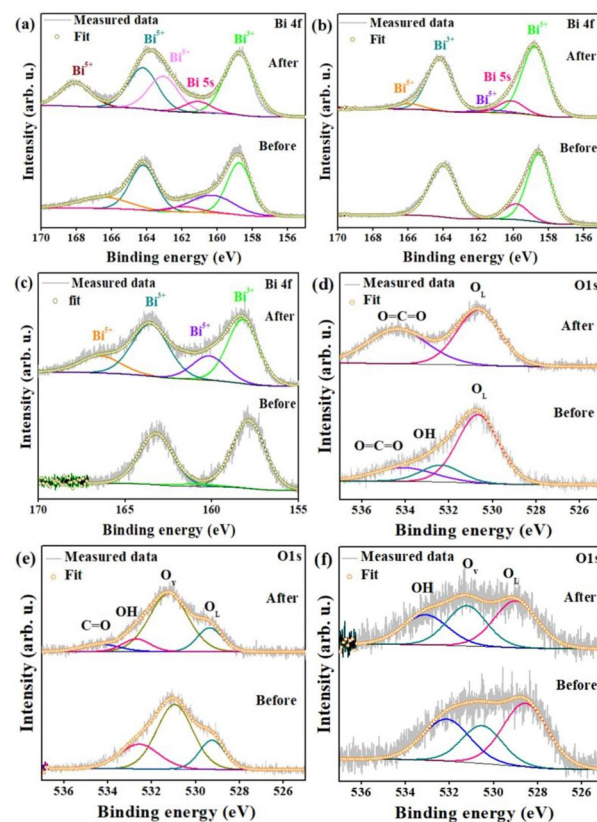


Fig. 8 Deconvoluted high resolution XPS spectra of Bi 4f and O 1s for (a) and (d) CBOC, (b) and (e) CBO and (c) and (f) BCO.

can be stated that oxygen vacancies were in a higher amount in the CBO, thus supporting its higher photocatalytic activity.

## Experimental

All the chemicals used in this work were of analytical grade and purchased from CentralChem s.r.o., Slovakia and Merck KGaA, Germany.

### Synthesis of Bi-based materials

The three different Bi-based materials, *i.e.*,  $\text{CaBi}_2\text{O}_2(\text{CO}_3)_2$ ,  $\text{Ca}_4\text{Bi}_6\text{O}_{13}$ , and  $\text{Bi}_2\text{Ce}_2\text{O}_7$ , were synthesized by previously reported procedures.<sup>35,36</sup>

### $\text{CaBi}_2\text{O}_2(\text{CO}_3)_2$ (CBOC)

For the synthesis of CBOC, 0.485 g of  $(\text{BiNO}_3)_3 \cdot 5\text{H}_2\text{O}$  was added to 10 mL ethylene glycol solution and kept under vigorous stirring at room temperature for 10 min. Subsequently, 0.118 g of  $\text{Ca}(\text{NO}_3)_2$  was slowly added to the solution. This reaction mixture transformed into a milky white colloidal suspension upon the incremental introduction of a 5 mL saturated solution of  $\text{K}_2\text{CO}_3$ . The suspension was stirred at room temperature for 30 min. Later, 15 mL of distilled water was added to the reaction mixture and was transferred into a solvothermal reactor. The vessel was heated at 140 °C for 72 h. After completion of the reaction, the white-coloured solid product



was separated by centrifugation, washed with distilled water until the washings reached a neutral pH, and finally dried at 60 °C overnight.<sup>35</sup>

### Ca<sub>4</sub>Bi<sub>6</sub>O<sub>13</sub> (CBO)

To synthesize CBO, 1.0 g of CaBi<sub>2</sub>O<sub>2</sub>(CO<sub>3</sub>)<sub>2</sub> (CBOC) was heated at 675 °C for 12 h in a crucible in a muffle furnace and then cooled down naturally to room temperature. A pale-yellow coloured product resulted after the heat treatment.

### Bi<sub>2</sub>Ce<sub>2</sub>O<sub>7</sub> (BCO)

BCO was synthesized using a hydroxide co-precipitation method. Typically, 0.4342 g of cerium nitrate (Ce(NO<sub>3</sub>)<sub>3</sub>·6H<sub>2</sub>O) dissolved in 5 ml distilled water and 0.4850 g of Bi(NO<sub>3</sub>)<sub>3</sub>·5H<sub>2</sub>O dissolved in a minimum amount of concentrated HNO<sub>3</sub> were mixed together. 1.2 M NaOH solution was incrementally added dropwise to the metal ion mixture until the pH reached 12. The resulting suspension was stirred for 6 h at room temperature. The solid precursor was separated through centrifugation and underwent repeated washing until the washings achieved a neutral pH. The solid was further dried in a hot air oven at 60 °C, and the dried product was calcined at 600 °C for 6 h.<sup>36</sup>

### Characterization techniques

All powder samples were subjected to powder X-ray diffraction (PXRD) using a PANalytical X-ray diffractometer equipped with CuK $\alpha$  radiation to confirm the phase purity. Furthermore, their lattice dimensions were determined by performing Le Bail refinements of the PXRD patterns using GSAS software.<sup>60,61</sup> The morphology of the samples was examined using scanning electron microscopy (SEM, Tescan Lyra III). The surface area measurements were recorded using BET (Brunauer–Emmett–Teller method, Sorptomatic 1990 SERIES, Thermo Quest CE Instruments, Italy) in the range of relative pressure  $p/p_0 = 0.05$ –0.25, and adsorption–desorption isotherms were measured at  $p/p_0 = 0$ –1, with the low-temperature adsorption method of N<sub>2</sub> at its boiling point of 77.7 K from vacuum to atmospheric pressure. The optical properties of the samples were measured by UV-VIS diffuse reflectance spectroscopy (DRS) using PerkinElmer Lambda-35 with a 50 mm integrating sphere and utilizing BaSO<sub>4</sub> as an external reference. The measured reflectance spectra were transformed by the Kubelka–Munk algorithm and the Tauc plot was applied to determine the energy of the band gap ( $E_g$ ).<sup>62</sup> In order to study surface chemistry of the samples before and after photocatalytic reactions, X-ray photo-electron spectroscopy (XPS, Omicron Nanotechnology, Mg K $\alpha$  photon energy 1253.6 eV) was used.

### Photoelectrochemical and work function measurements

All three samples were investigated for photocurrent generation, incident photon-to-current efficiency (IPCE) and work function measurements. The photoelectrochemical properties were determined using a photoelectric spectrometer (Instytut Fotonowy, Krakow, Poland), and the work function was measured using a Kelvin probe (Instytut Fotonowy, Krakow, Poland).

Photoelectrochemical measurements were performed using a photoelectric spectrometer and a three-electrode configuration, with Ag/AgCl and platinum wire as the reference and counter electrode. A thin layer of the analyte material deposited on ITO-coated transparent PET foil (60 Ω sq<sup>-1</sup> resistance, Sigma-Aldrich) served as a working electrode. The working electrode was prepared by the following procedure: 20 mg of the sample was finely ground in an agate mortar, 150 mL of ethanol was added afterward and the suspension was stirred in an Eppendorf using a Shaker Vortex mixer ZX4 (Velpsa) for 15 min. A thin layer was made from the suspension using an Elcometer Micrometric film applicator (Elcometer 3570/1, Great Britain). The ITO foil was washed with ethanol and dried at 80 °C before the deposition of the thin layer. The deposited uniform film was then dried at 80 °C in a dryer. The 0.1 mol L<sup>-1</sup> KNO<sub>3</sub> solution (pH = 6.1) was used as an electrolyte. The electrolyte was purged to remove oxygen by argon before the photocurrent measurements for 15 min. Argon flow was kept constant during the entire experiment. Photocurrents were recorded by irradiating the working electrode from the backside with a xenon lamp (150 W) in the range of 250–450 nm with a 10 nm step (controlled by a monochromator) and by applying voltages in the range between –0.2 and 1.0 V (vs. Ag/AgCl). The size of the working electrode is determined by the diameter of the window (1.0 cm) and the irradiated surface area is 0.785 cm<sup>2</sup>.

Work function measurements were conducted using a Kelvin probe. The technique consists of the measurements of contact potential difference (CPD) between the oscillating reference electrode made of a gold grid (also referenced as a tip) of a known work function (5.1 eV) and the working electrode (measured sample) of an unknown work function. The obtained CPD is given by the difference in work functions of the tip and the sample (eqn (6)). Therefore, the work function of the sample is calculated according to eqn (7).

$$\text{CPD} = \Phi_{\text{sample}} - \Phi_{\text{tip}} \quad (6)$$

$$\Phi_{\text{sample}} = \text{CPD} + \Phi_{\text{tip}} \quad (7)$$

During the CPD measurement, the whole system was placed in a grounded Faraday cage to reduce the electrical noise and the influence of stray light. Temperature and humidity inside the Faraday cage were monitored during the entire measurement. 100 mg of the sample was pressed into a pellet under 100 MPa. The work function was measured from minimally 5 different spots of the pellet. The final value was determined as the average work function from these spots.

### Photocatalytic decomposition of N<sub>2</sub>O

Photocatalytic N<sub>2</sub>O decomposition experiments were implemented in a batch photoreactor (200 mL). Initially, 0.1 g of powder photocatalyst was positioned uniformly at the bottom of the batch photoreactor to maximize the contact surface. Subsequently, the reactor was filled with the mixture of N<sub>2</sub>O/He (concentration of N<sub>2</sub>O = 1030 ppm) and exposed to a polychromatic UV-A (Ultraviolet Products Inc.,  $\lambda_{\text{max}} = 365$  nm) or UV-C (Ultraviolet Products Inc.,  $\lambda_{\text{max}} = 254$  nm) pen-ray lamp (Fig. S5 (ESI<sup>†</sup>)). The selected source was situated on a quartz glass



window on top of the photoreactor in a horizontal position. Prior to initiating the reaction, a gaseous sample was taken (at 0 h) through the septum by a gastight syringe. The gaseous samples were analysed by a gas chromatograph (Shimadzu Tracera GC-2010Plus) equipped with a BID (barrier discharge ionization detector). The reaction mixture was irradiated at intervals of 0–24 h with a sampling frequency of 2 h. All measurements were repeated with the resulted error below 5%. The stability of the investigated samples was demonstrated by repeated use of the same batch, yielding consistent results. A reduction in  $\text{N}_2\text{O}$  concentration and an increase in the ratio of oxygen and nitrogen were observed.

## Conclusions

This study emphasized the successful synthesis of CBOC, CBO, and BCO and their exploration in the photocatalytic decomposition of  $\text{N}_2\text{O}$  for the first time. The Bi-based materials' photoelectrochemical properties and work function confirmed that they can be photoactivated under UVA light. The highest photocurrent generation was achieved in the presence of the CBO sample and reached  $0.09 \mu\text{A}$  at 1 V and 365 nm (with an IPCE of 0.4%), which is 4.5-fold and 10-fold higher than for CBOC and BCO. CBO also exhibited the highest performance in photocatalytic decomposition of  $\text{N}_2\text{O}$ , where 10.4% was removed after 24 h under UV-A light. Although CBO has the smallest surface area, its photocatalytic performance highlights the complex combination of several properties with different impacts. In the present case, the electronic properties have a predominant role compared to the surface properties. The mechanistic aspect was also deduced, and the enhanced  $\text{N}_2\text{O}$  decomposition using CBO was due to oxygen vacancies. This work underscores that the investigated Bi-based materials are promising solar-light driven photocatalysts as (i) UVA is a part of natural sunlight and (ii) optimization of optical and electronic properties brought by Bi could harness also the visible part of the solar spectrum. Therefore, this work is an added-value in the fundamental understanding of Bi-based materials in photocatalytic processes and it highlights that further investigations are necessary to maximize their responsiveness and effectiveness under continuous sunlight exposure.

## Author contributions

Shalu Atri: conceptualization – investigation – methodology – writing: original draft – writing: review & editing – funding acquisition; Sitharaman Uma: conceptualization – visualization – writing: review & editing; Rajamani Nagarajan: investigation – visualization – writing: review & editing; Maros Gregor: investigation; Tomas Roch: investigation; Miroslava Filip Edelmannová – investigation, Martin Reli – investigation, Kamila Koci: supervision – funding acquisition; Martin Motola: writing: review & editing – funding acquisition; Olivier Monfort: conceptualization – supervision – writing: original draft – writing: review & editing – funding acquisition.

## Data availability

Data cannot be made available due to legal confidentiality requirements.

## Conflicts of interest

There are no conflicts to declare.

## Acknowledgements

This work has been carried out in the frame of the PhotoMXene project No. 3305/03/02 co-funded by the EU Horizon 2020 Research and Innovation Program under the Program SASPRO2 COFUND Marie Skłodowska-Curie grant agreement No. 945478. This research has also been partially supported by the Slovak Research and Development Agency (Contract No. APVV-21-0039) and the Scientific Grant Agency of the Slovak Republic (VEGA project No. 1/0319/23). The work was also supported by the Large Research Infrastructure ENREGAT (project No. LM2023056). The authors thank Hryhorii Makarov for the SEM pictures.

## References

- 1 N. Pasha, P. S. S. Reddy, T. V. Sagar, N. Lingaiah and P. S. Prasad, Combating Global Warming due to Nitrous Oxide, *Sci. Spectra*, 2016, **1**, 410–423.
- 2 H. Y. Chen, Z. H. Wei, M. Kollar, F. Gao, Y. L. Wang, J. Szanyi and C. H. F. Peden, A comparative study of  $\text{N}_2\text{O}$  formation during the selective catalytic reduction of  $\text{NO}_x$  with  $\text{NH}_3$  on zeolite supported Cu catalysts, *J. Catal.*, 2015, **329**, 490–498.
- 3 G. Grzybek, S. Wojcik, P. Legutko, J. Grybos, P. Indyka, B. Leszczynski, A. Kotarba and Z. Sojka, Thermal stability and repartition of potassium promoter between the support and active phase in the  $\text{K}-\text{Co}_{2.6}\text{Zn}_{0.4}\text{O}_4$  vertical bar alpha- $\text{Al}_2\text{O}_3$  catalyst for  $\text{N}_2\text{O}$  decomposition: Crucial role of activation temperature on catalytic performance, *Appl. Catal., B*, 2017, **205**, 597–604.
- 4 M. Jablonska and R. Palkovits, It is no laughing matter: nitrous oxide formation in diesel engines and advances in its abatement over rhodium-based catalysts, *Catal. Sci. Technol.*, 2016, **6**(21), 7671–7687.
- 5 C. Zhang, Z. Zhang, C. Sui, F. Yuan, X. Niu and Y. Zhu, Catalytic decomposition of  $\text{N}_2\text{O}$  over Co-Ti oxide catalysts: Interaction between Co and Ti oxide, *ChemCatChem*, 2016, **8**, 2155–2164.
- 6 C. Pophal, T. Yogo, K. Yamada and K. Segawa, Selective catalytic reduction of nitrous oxide over Fe-MFI in the presence of propene as reductant, *Appl. Catal., B*, 1998, **16**, 177–186.
- 7 A. Y. Wang, Y. L. Wang, E. D. Walter, R. K. Kukkadapu, Y. L. Guo, G. Z. Lu, R. S. Weber, Y. Wang, C. H. F. Peden and F. Gao, Catalytic  $\text{N}_2\text{O}$  decomposition and reduction by  $\text{NH}_3$  over Fe/Beta and Fe/SSZ-13 catalysts, *J. Catal.*, 2018, **358**, 199–210.



8 M. Konsolakis, Recent advances on nitrous oxide ( $N_2O$ ) decomposition over non-noble-metal oxide catalysts: Catalytic performance, mechanistic considerations, and surface chemistry aspects, *ACS Catal.*, 2015, **5**, 6397–6421.

9 R. J. Stella, I. Sreevani, T. R. Gurugubelli, R. V. S. S. N. Ravikumar and R. Koutavarapu, Enhanced Solar Light-Driven Photocatalytic Degradation of Tetracycline Using  $Fe^{3+}$ -Doped CdO/ZnS Nanocomposite: Mechanistic Insights and Performance Evaluation, *Catalysts*, 2023, **13**(9), 1312.

10 K. Koci, M. Reli, I. Troppova, M. Sihor, J. Kupkova, P. Kustrowski and P. Praus, Photocatalytic decomposition of  $N_2O$  over  $TiO_2/g-C_3N_4$  photocatalysts heterojunction, *Appl. Surf. Sci.*, 2017, **396**, 1685–1695.

11 L. Matejova, M. Sihor, J. Lang, I. Troppova, N. Ambrozova, M. Reli, T. Brunatova, L. Capek, A. Kotarba and K. Koci, Investigation of low Ce amount doped- $TiO_2$  prepared by using pressurized fluids in photocatalytic  $N_2O$  decomposition and  $CO_2$  reduction, *J. Sol-Gel Sci. Technol.*, 2017, **84**, 158–168.

12 Q. Wu, C.-C. Yang and R. van de Krol, A dopant-mediated recombination mechanism in Fe-doped  $TiO_2$  nanoparticles for the photocatalytic decomposition of nitric oxide, *Catal. Today*, 2014, **225**, 96–101.

13 D. P. Dutta, M. Roy and A. K. Tyagi, Dual function of rare earth doped nano  $Bi_2O_3$ : white light emission and photocatalytic properties, *Dalton Trans.*, 2012, **41**, 10238–10248.

14 Z. Wu, Y. Shen, A. Xie, F. Huang, Y. Cai and S. Lie, Sonochemical fabrication and optical properties of  $ZnO$  tilliform dendrites containing  $Bi_2O_3$ , *Indian J. Chem.*, 2009, **48A**, 51–56.

15 L. Cheng and Y. Kang, Selective preparation of  $Bi_2O_3$  visible light driven photocatalyst by dispersant and calcination, *J. Alloys Compd.*, 2014, **585**, 85–93.

16 Z. Ai, Y. Huang, S. Lee and L. Zhang, Monoclinic  $\alpha$ - $Bi_2O_3$  photocatalyst for efficient removal of gaseous NO and  $HCHO$  under visible light irradiation, *J. Alloys Compd.*, 2011, **509**, 2044–2049.

17 J. Wei, C. Cai, S. Xu and Y. Zhang, Synthesis and characterization of a pigment with a high near-infrared reflectance:  $Ca^{2+}$ -doped  $Bi_2O_3$ , *Ceram. Int.*, 2024, **50**(4), 6606–6614.

18 S. Akshatha, S. Sreenivasa, L. Parashuram, V. U. Kumar, S. C. Sharma, H. Nagabhushana, S. Kumar and T. Maiyalagan, Synergistic effect of hybrid  $Ce^{3+}/Ce^{4+}$  doped  $Bi_2O_3$  nano-sphere photocatalyst for enhanced photocatalytic degradation of alizarin red S dye and its NUV excited photoluminescence studies, *J. Environ. Chem. Eng.*, 2019, **7**(3), 103053.

19 Y. Bi, R. Li, F. Guo, C. Zhu and J. Pei, Photocatalytic purification of vehicle exhaust using  $CeO_2$ - $Bi_2O_3$  loaded on white carbon and tourmaline, *Environ. Sci. Pollut. Res.*, 2021, **28**, 17724–17738.

20 S. T. Aziz, M. Ummekar, I. Karajagi, S. K. Riyajuddin, K. V. Siddhartha, A. Saini, A. Potbhare, R. G. Chaudhary, V. Vishal, P. C. Ghosh and A. Dutta, A Janus cerium-doped bismuth oxide electrocatalyst for complete water splitting, *Cell Rep. Phys. Sci.*, 2022, **3**(11), 101106.

21 K. Masula, Y. Bhongiri, G. R. Rao, P. V. Kumar, S. Pola and M. Basude, Evolution of photocatalytic activity of  $CeO_2$ - $Bi_2O_3$  composite material for wastewater degradation under visible-light irradiation, *Opt. Mater.*, 2022, **126**, 112201.

22 S. Liu, J. Sun, G. Ren and X. Meng, Vacancy-engineered bismuth-based semiconductor with enhanced photocatalytic activity: A review, *Mater. Sci. Semicond. Process.*, 2022, **137**, 106230.

23 P. Chen, H. Liu, W. Cui, S. C. Lee, L. A. Wang and F. Dong, Bi-based photocatalysts for light-driven environmental and energy applications: structural tuning, reaction mechanisms, and challenges, *EcoMat*, 2020, **2**(3), e12047.

24 K. Qin, Q. Zhao, H. Yu, X. Xia, J. Li, S. He, L. Wei and T. An, A review of bismuth-based photocatalysts for antibiotic degradation: Insight into the photocatalytic degradation performance, pathways and relevant mechanisms, *Environ. Res.*, 2021, **199**, 111360.

25 T. L. Wakjira, A. B. Gemta, G. B. Kassahun, D. M. Andoshe and K. Tadele, Bismuth-Based Z-Scheme Heterojunction Photocatalysts for Remediation of Contaminated Water, *ACS Omega*, 2024, **9**(8), 8709–8729.

26 H. Kunioku, M. Higashi, O. Tomita, M. Yabuuchi, D. Kato, H. Fujito, H. Kageyama and R. Abe, Strong hybridization between  $Bi$ -6s and  $O$ -2p orbitals in Sillen-Aurivillius perovskite  $Bi_4MO_8X$  ( $M$ = Nb, Ta;  $X$ = Cl, Br), visible light photocatalysts enabling stable water oxidation, *J. Mater. Chem. A*, 2018, **6**(7), 3100–3107.

27 H. Huang, C. Zhou, X. Jiao, H. Yuan, J. Zhao, C. He, J. Hofkens, M. B. J. Roeffaers, J. Long and J. A. Steele, Subsurface defect engineering in single-unit-cell  $Bi_2WO_6$  monolayers boosts solar driven photocatalytic performance, *ACS Catal.*, 2020, **10**(2), 1439–1443.

28 A. Walsh, D. J. Payne, R. G. Egisdell and G. W. Watson, Stereochemistry of post-transition metal oxides: revision of the classical lone pair model, *Chem. Soc. Rev.*, 2011, **40**(9), 4455–4463.

29 J. Wu, K. Xu, Q. Z. Liu, Z. Ji, C. H. Qu, X. Qi, H. Zhang, Y. Guan, P. He and L. J. Zhu, Controlling dominantly reactive (010) facets and impurity level by *in situ* reduction of  $BiOIO_3$  for enhancing photocatalytic activity, *Appl. Catal. B*, 2018, **232**, 135–145.

30 X. Liao, X. Lan, N. Ni, P. Yang, Y. Yang and X. Chen, Bismuth oxychloride nanowires for photocatalytic decomposition of organic dyes, *ACS Appl. Nano Mater.*, 2021, **4**(4), 3887–3892.

31 J. D. Grice, A solution to the crystal structures of bismutite and beyerite, *Can. Mineral.*, 2002, **40**(2), 693–698.

32 J. Kawano, S. Maeda and T. Nagai, The effect of  $Mg^{2+}$  incorporation on the structure of calcium carbonate clusters: investigation by the anharmonic downward distortion following method, *Phys. Chem. Chem. Phys.*, 2016, **18**(4), 2690–2698.

33 L. Yu, D. Li, S. Zhao, G. Li and K. Yang, First principles study on electronic structure and optical properties of ternary  $GaAs$ :  $Bi$  alloy, *Materials*, 2012, **5**(12), 2486–2497.

34 S. A. Paramita, I. Nurhasanah and A. Khumaeni, Structural and Optical Properties of Bismuth Doped Cerium Oxide



Prepared at Low temperature, *J. Penelit. Fis. Apl.*, 2023, **13**(1), 16–24.

35 V. Malik, M. Pokhriyal and S. Uma, Single step hydrothermal synthesis of beyerite,  $\text{CaBi}_2\text{O}_2(\text{CO}_3)_2$  for the fabrication of UV-visible light photocatalyst  $\text{BiOI/CaBi}_2\text{O}_2(\text{CO}_3)_2$ , *RSC Adv.*, 2016, **6**(44), 38252–38262.

36 S. Uniyal, S. Atri, S. Uma and R. Nagarajan, Microstructural changes caused by Ba and Pr doping in nanosized  $\text{Bi}_2\text{Ce}_2\text{O}_7$  leading to interesting optical, magnetic, and catalytic properties., *CrystEngComm*, 2021, **23**(4), 986–999.

37 K. Obata, K. Matsumoto, T. Uehara, A. Doi, Y. Obukuro and S. Matsushima, Preparation and characterization of  $\text{Ca}_4\text{Bi}_6\text{O}_{13}$  complex oxide., *Chem. Lett.*, 2011, **40**(3), 288–289.

38 S. Atri, V. Malik, S. Uma and R. Nagarajan, Catalytic applications of mesoporous  $\text{CaBi}_2\text{O}_4$  obtained from a single source precursor., *Res. Chem. Intermed.*, 2019, **45**, 2457–2470.

39 D. B. Hernandez-Uresti, D. Sanchez-Martínez, A. Martinez-de La Cruz, S. Sepulveda-Guzman and L. M. Torres-Martinez, Characterization and photocatalytic properties of hexagonal and monoclinic  $\text{WO}_3$  prepared via microwave-assisted hydrothermal synthesis, *Ceram. Interfaces*, 2014, **40**(3), 4767–4775.

40 S. Brunauer, P. H. Emmett and E. Teller, Adsorption of gases in multimolecular layers, *J. Am. Chem. Soc.*, 1938, **60**(2), 309–319.

41 L. Gurvitsch, Physicochemical attractive force, *J. Phys. Chem. Soc.*, 1915, **47**, 805–827.

42 G. Horvath and K. Kawazoe, Method for the calculation of effective pore size distribution in molecular sieve carbon, *J. Chem. Eng.*, 1983, **16**(6), 470–475.

43 E. P. Barrett, L. G. Joyner and P. P. Halenda, The determination of pore volume and area distributions in porous substances. I. Computations from nitrogen isotherms, *J. Am. Chem. Soc.*, 1951, **73**(1), 373–380.

44 B. C. Lippens and J. H. De Boer, Studies on pore systems in catalysts: V. The t method, *J. Catal.*, 1965, **4**(3), 319–323.

45 H. Zhu, M. Pan, M. B. Johansson and E. M. Johansson, High photon-to-current conversion in solar cells based on light-absorbing silver bismuth iodide, *ChemSusChem*, 2017, **10**(12), 2592–2596.

46 P. Stelmachowski, G. Maniak, A. Kotarba and Z. Sojka, Strong electronic promotion of  $\text{Co}_3\text{O}_4$  towards  $\text{N}_2\text{O}$  decomposition by surface alkali dopants., *Catal. Commun.*, 2009, **10**(7), 1062–1065.

47 F. Bosca, P. Morliere, M. A. Miranda, J. V. Castell and R. Santus, Primary steps of the photochemical reactions of 2-cyano-10-(3-[dimethylamino, N-oxide]-2-methylpropyl)-5-oxide-phenothiazine, the photoproduct of cyamemazine, a phototoxic neuroleptic: comparison with the sulfoxide, *Photochem. Photobiol. Sci.*, 2006, **5**, 336–342.

48 K. Koci, M. Reli, I. Troppova, M. Sihor, J. Kupkova, P. Kustrowski and P. Praus, Photocatalytic decomposition of  $\text{N}_2\text{O}$  over  $\text{TiO}_2/\text{g-C}_3\text{N}_4$  photocatalysts heterojunction., *Appl. Surf. Sci.*, 2017, **396**, 1685–1695.

49 K. Koci, M. Reli, I. Troppova, M. Sihor, T. Bajcarova, M. Ritz, J. Pavlovsky and P. Praus, Photocatalytic decomposition of  $\text{N}_2\text{O}$  by using nanostructured graphitic carbon nitride/zinc oxide photocatalysts immobilized on foam, *J. Catal.*, 2019, **9**(9), 735.

50 K. Koci, S. Krejcikova, O. Solcova and L. Obalova, Photocatalytic decomposition of  $\text{N}_2\text{O}$  on  $\text{Ag-TiO}_2$ , *Catal. Today*, 2012, **191**(1), 134–137.

51 M. Reli, I. Troppova, M. Sihor, J. Pavlovsky, P. Praus and K. Koci, Photocatalytic decomposition of  $\text{N}_2\text{O}$  over  $\text{g-C}_3\text{N}_4/\text{BiVO}_4$  composite., *Appl. Surf. Sci.*, 2019, **469**, 181–191.

52 J. Tan, H. Cheng, J. Liu, J. Sun, Y. Li, H. Wang, J. Liu and Z. Zhao, Room-Temperature Photocatalytic Decomposition of  $\text{N}_2\text{O}$  over Nanobel-Like  $\text{Bi}_2\text{MoO}_6$ , *ChemistrySelect*, 2019, **4**(18), 5338–5344.

53 K. Koci, I. Troppova, M. Reli, L. Matejova, M. Edelmannova, H. Drobna, L. Dubnova, A. Rokicinska, P. Kustrowski and L. Capek,  $\text{Nd/TiO}_2$  anatase-brookite photocatalysts for photocatalytic decomposition of methanol, *Front. Chem.*, 2018, **6**, 1–11.

54 A. Kudo and H. Nagayoshi, Photocatalytic reduction of  $\text{N}_2\text{O}$  on metal-supported  $\text{TiO}_2$  powder at room temperature in the presence of  $\text{H}_2\text{O}$  and  $\text{CH}_3\text{OH}$  vapor, *Catal. Lett.*, 1998, **52**, 109–111.

55 N. Richards, L. A. Parker, J. H. Carter, S. Pattisson, D. J. Morgan, N. F. Dummer, S. E. Golunski and G. J. Hutchings, Effect of the Preparation Method of  $\text{LaSr-CoFeO}_x$  Perovskites on the Activity of  $\text{N}_2\text{O}$  Decomposition., *Catal. Lett.*, 2022, 1–14.

56 Y. Zhang, D. Li, Y. Zhang, X. Zhou, S. Guo and L. Yang, Graphene-wrapped  $\text{Bi}_2\text{O}_2\text{CO}_3$  core-shell structures with enhanced quantum efficiency profit from an ultrafast electron transfer process, *J. Mater. Chem. A*, 2014, **2**(22), 8273–8280.

57 R. Zalecki, W. Woch, M. Kowalik, A. Kołodziejczyk and G. Gritzner, Bismuth Valence in a  $\text{Tl}_{0.7}\text{Bi}_{0.3}\text{Sr}_{1.6}\text{Ba}_{0.4}\text{Ca-Cu}_2\text{O}_y$  Superconductor from X-Ray Photoemission Spectroscopy, *Acta Phys. Pol. A*, 2010, **118**(2), 393–395.

58 Z. Li, M. Wang, J. Shen, Z. Zhu and Y. Liu, Synthesis of  $\text{BiOI}$  nanosheet/coarsened  $\text{TiO}_2$  nanobel heterostructures for enhancing visible light photocatalytic activity., *RSC Adv.*, 2016, **6**(36), 30037–30047.

59 D. S. Shin, H. G. Kim, H. S. Ahn, H. Y. Jeong, Y. J. Kim, D. Odkhui, N. Tsogbadrakh and B. H. Kim, Distribution of oxygen functional groups of graphene oxide obtained from low-temperature atomic layer deposition of titanium oxide, *RSC Adv.*, 2017, **7**(23), 13979–13984.

60 A. C. Larson and R. B. Von Dreele, General Structure Analysis System (GSAS), Los Alamos National Laboratory Report LAUR, 2004, pp. 86–748.

61 B. H. Toby, EXPGUI, a Graphical User Interface for GSAS, *J. Appl. Crystallogr.*, 2001, **34**, 210.

62 P. Makuła, M. Pacia and W. Macyk, How to correctly determine the band gap energy of modified semiconductor photocatalysts based on UV-Vis spectra, *J. Phys. Chem. Lett.*, 2018, **9**(23), 6814–6817.

